scientific reports

Check for updates

OPEN

Water mediated growth of oriented single crystalline $SrCO_3$ nanorod arrays on strontium compounds

Junsung Hong[1,2], Su Jeong Heo[1,3] & Prabhakar Singh[1]✉

Morphology-controlled strontianite nanostructures have attracted interest in various fields, such as electrocatalyst and photocatalysts. Basic additives in aqueous strontium solutions is commonly used in controlling strontianite nanostructures. Here, we show that trace water also serves an important role in forming and structuring vertically oriented strontianite nanorod arrays on strontium compounds. Using in situ Raman spectroscopy, we monitored the structural evolution from hydrated strontium to strontianite nanorods, demonstrating the epitaxial growth by vapor–liquid–solid mechanism. Water molecules cause not only the exsolution of Sr liquid droplets on the surface but also the uptake of airborne CO_2 followed by its ionization to CO_3^{2-}. The existence of intermediate $SrHO^+$–OCO_2^{2-} phase indicates the interaction of CO_3^{2-} with $SrOH^+$ in $Sr(OH)_x(H_2O)_y$ cluster to orient strontianite crystals. X-ray diffraction simulation and transmission electron microscopy identify the preferred-orientation plane of the 1D nanostructures as the (002) plane, i.e., the growth along the c-axis. The anisotropic growth habit is found to be affected by the kinetics of carbonation. This study paves the way for designing and developing 1D architecture of alkaline earth metal carbonates by a simple method without external additives at room temperature.

Strontium is an alkaline earth metal that has two electrons in the outer valence shell. It has a very low electronegativity (1.0), thus tending to be readily ionized as Sr^{2+} to react with oxygen and H_2O in air[1]. It is an important element as A-site dopant or ingredient in perovskite-type electrodes and catalysts[2–4]. For instance, in (La,Sr)MnO_3 and (La,Sr)(Co,Fe)O_3 perovskite cathodes, the Sr^{2+} substitution for La^{3+} provides a structure that is favorable to polaron hopping, improving the electrical conductivity in solid oxide fuel cells (SOFC)[5–8].

Sr surface segregation frequently occurs in perovskite structures and is among important issues since the near-surface structure determines the overall properties of the materials. The relatively large size of Sr^{2+} (0.144 nm for 12 coordination) is regarded as the cause of the segregation[9–14]. In humid environments, the segregation is accelerated as the absorption of H_2O distorts the lattice, allowing for facile migration of Sr ions toward the surface[15–17]. The segregated Sr is likely to exist as $SrCO_3$ on the surface[18].

Strontianite, or $SrCO_3$, has a wide range of applications, such as in dye-sensitized solar cell[19], thermochemical energy storage[20], cataluminescence-based sensor[21], eletrocatalyst[22], and photocatalyst[23–25], apart from raw material in industry. The morphology control of $SrCO_3$ has attracted considerable interest as providing the opportunity to explore and develop novel properties: e.g., urchin-like $SrCO_3$ particles showed enhanced specific capacitance[26], and vertically-oriented $SrCO_3$ nanorods exhibited photoluminescence (PL) quenching over the full solar spectrum range[27].

In fabricating $SrCO_3$ hierarchical superstructures (e.g., needle-, dumbbell-, and flower-like morphologies), various synthesis methods including hydrothermal route have been developed, where strontium nitrate, chloride, and acetate are frequently used as the Sr source (listed in Supplementary Table S1 online)[26–42]. Our recent work showed that the continuous Sr segregation induced by H_2O absorption leads to the formation of $SrCO_3$ (Supplementary Fig. S1 online), especially with nanorod morphology[16]. However, no report has been found for the $SrCO_3$ formation via the H_2O absorption induced Sr-segregation in ambient environment, which could be closely related to the biomineral carbonation in nature. Despite great advances in the synthesis and application, studies on the fundamental science of $SrCO_3$ formation have lagged behind. For further design and development of one-dimensional (1D) architectures of $SrCO_3$, the growth mechanism of $SrCO_3$ nanorods needs to be understood.

[1]Department of Materials Science and Engineering, University of Connecticut, Storrs, CT 06269, USA. [2]Present address: Department of Materials Science and Engineering, Northwestern University, Evanston, IL 60208, USA. [3]Present address: Materials Science Center, National Renewable Energy Laboratory, Golden, CO 80401, USA. ✉email: prabhakar.singh@uconn.edu

The current study focuses on the structuring role of water in the growth of single-crystalline $SrCO_3$ nanorod arrays. The evolution of hydrated strontium into $SrCO_3$ is investigated by in situ Raman spectroscopy. It is found that the hydrated Sr has a strong tendency to absorb CO_2 in air whereas non-hydrated Sr does not. The observation of the intermediate phase, as well as thermodynamic considerations, elucidates the reaction pathway for the formation of $SrCO_3$. X-ray diffraction (XRD) simulation and transmission electron microscopy (TEM) analyses further reveal that the epitaxial growth of $SrCO_3$ occurs along the *c*-axis, leaving stacking faults behind.

Results

$SrCO_3$ vertical growth on hydrated strontium compounds. As an example, $Sr_9Ni_7O_{21}$, which is one of Sr-enriched structures and subject to Sr segregation in humid environment, was used to investigate the growth of $SrCO_3$ nanorods from hydrated strontium compounds. Figure 1a shows scanning electron microscopy (SEM) images of the surface of strontium nickel oxide (SNO; $Sr_9Ni_7O_{21}$) exposed to a humid environment (2.7% H_2O) for 0–48 h and 10 days. It is seen that Sr is readily segregated from SNO by absorbing moisture, leading to the growth of nanorods on the surface. Figure 1b displays the cross-sectional images (HAADF and elemental mapping) of the nanorods on the SNO surface. Sr-enrichment is observed in the surface nanorods and along the SNO grain boundaries. The nanorod is identified as $SrCO_3$ (*Pmcn*; JCPDS No. 05-0418) by the fast-Fourier-transform (FFT) technique (Fig. 1c), thus demonstrating Sr-segregation and $SrCO_3$ growth from a Sr-rich compound. It should be noted that the strontium, segregated by H_2O absorption, would exist initially as $Sr(OH)_2{\cdot}8H_2O$, according to our previous study[16]. The hydrated Sr-hydroxide is subject to reacting with CO_2 in air, resulting in $SrCO_3$, as per the reaction.

$$Sr(OH)_2 \cdot 8H_2O + CO_{2(g)} \rightarrow SrCO_3 + 9H_2O \quad (1)$$

It is interesting that the $SrCO_3$ here grows in one-dimension, eventually forming $SrCO_3$ nanorod arrays on the SNO surface (Fig. 1d). Such a phenomenon may occur in other alkaline-earth-metal compounds as well. For instance, $SrCO_3$ nanowhiskers were found to grow from $Sr_4Mn_3O_{10}$ in humid environment (see Supplementary Fig. S4 online), which have potential applications as Cr/S getters[43] in high-temperature electrochemical systems. While water molecules are considered contributors to the directional growth, the role of water molecules in Sr carbonation is rarely studied. It remains to be discovered how $Sr(OH)_2{\cdot}8H_2O$ in air transforms into $SrCO_3$ and how the resultant $SrCO_3$ has 1D morphology. These questions will be answered in the following sections.

Effect of moisture on $SrCO_3$ formation. In order to study the influence of moisture on the formation of $SrCO_3$, as-received SrO and $Sr(OH)_2{\cdot}8H_2O$ powders were placed for 24 h in an ambient room air (1.2% H_2O present; and 400 ppm CO_2) or under a flow of CO_2–air mixed gas (H_2O absent; and 30% CO_2). Their morphology and structure changes were analyzed by SEM and XRD.

Figure 2 displays XRD patterns and SEM images of the SrO exposed to the two different atmospheric conditions. Several distinguishing characteristics of the reactivity of SrO with air were revealed as follows. First, as-received SrO (Alfa Aesar, USA) was identified as $Sr(OH)_2{\cdot}H_2O$ with a small portion of $Sr(OH)_2$ by XRD analysis (Fig. 2a) since SrO was readily hydrated by absorbing airborne moisture during the XRD analysis, indicating the hygroscopic nature of SrO. Second, it is interesting that SrO (and if any existing $Sr(OH)_2$) does not react with airborne CO_2 in the absence of moisture; that is, no $SrCO_3$ formed under dry CO_2–air flow, albeit containing a high concentration of CO_2 (30%) (Fig. 2b,d). In other words, the reaction between SrO and CO_2 occurs only in the presence of moisture; indeed, $SrCO_3$ was produced in an ambient air containing moisture (1.2% H_2O in this case) although the concentration of CO_2 was as low as 400 ppm (Fig. 2c). Third, a morphological transformation into nanorods during the $SrCO_3$ formation was observed (Fig. 2e). Further information to understand the anisotropic growth of $SrCO_3$ is given in Fig. 3.

Figure 3 shows XRD patterns and SEM images of the $Sr(OH)_2{\cdot}8H_2O$ exposed to the two different atmospheric conditions. It is found that the exposure of hydrated strontium (i.e., $Sr(OH)_2{\cdot}8H_2O$) to CO_2, regardless of the presence of moisture, results in the formation of $SrCO_3$ (Fig. 3a–c), corresponding to the above discussion. SEM observations reveal that the $SrCO_3$ tends to grow in one-dimension when derived from $Sr(OH)_2{\cdot}8H_2O$ (Fig. 3d,e). This tendency is very prominent for the $Sr(OH)_2{\cdot}8H_2O$ exposed to air containing moisture (Fig. 3e). That is, quasi-vertically aligned $SrCO_3$ nanorod arrays were produced from the $Sr(OH)_2{\cdot}8H_2O$ further hydrated in the presence of moisture (i.e., 1.2% H_2O with 400 ppm CO_2 in an ambient air) (Fig. 3e) whereas irregularly aligned $SrCO_3$ nanorods with relatively small aspect ratios grew in the moisture-free environment (i.e., dry air with 30% CO_2) (Fig. 3d).

The anisotropic growth of $SrCO_3$ from $Sr(OH)_2{\cdot}8H_2O$ in air can be explained by considering the reaction kinetics. As per Eq. (1), in the very low partial pressure of CO_2 (i.e., 400 ppm in air), the reaction rate for $SrCO_3$ formation would be very slow, so that the clusters and nuclei of $SrCO_3$ afford movement and rotation to assemble along their preferential orientation, resulting in the 1D-oriented growth of $SrCO_3$. This is possible because moisture can hydrate the surface strontium and form an aqueous liquid layer over the solid crystalline $Sr(OH)_2{\cdot}8H_2O$ where $SrCO_3$ nuclei can move and rotate freely; indeed, the presence of aqueous liquid layer on SNO surface was found (see Supplementary Fig. S3 online).

Preferred growth orientation of $SrCO_3$. The preferred orientation for the growth of $SrCO_3$ is further investigated by XRD simulations together with the measured XRD data. First, the XRD pattern of the quasi-vertically aligned $SrCO_3$ nanorod arrays in Fig. 3c was closely inspected. The intensity of (111) peak is the strongest while that of (021) peak seems to be weakened, compared with Fig. 3b. This has often misled us to

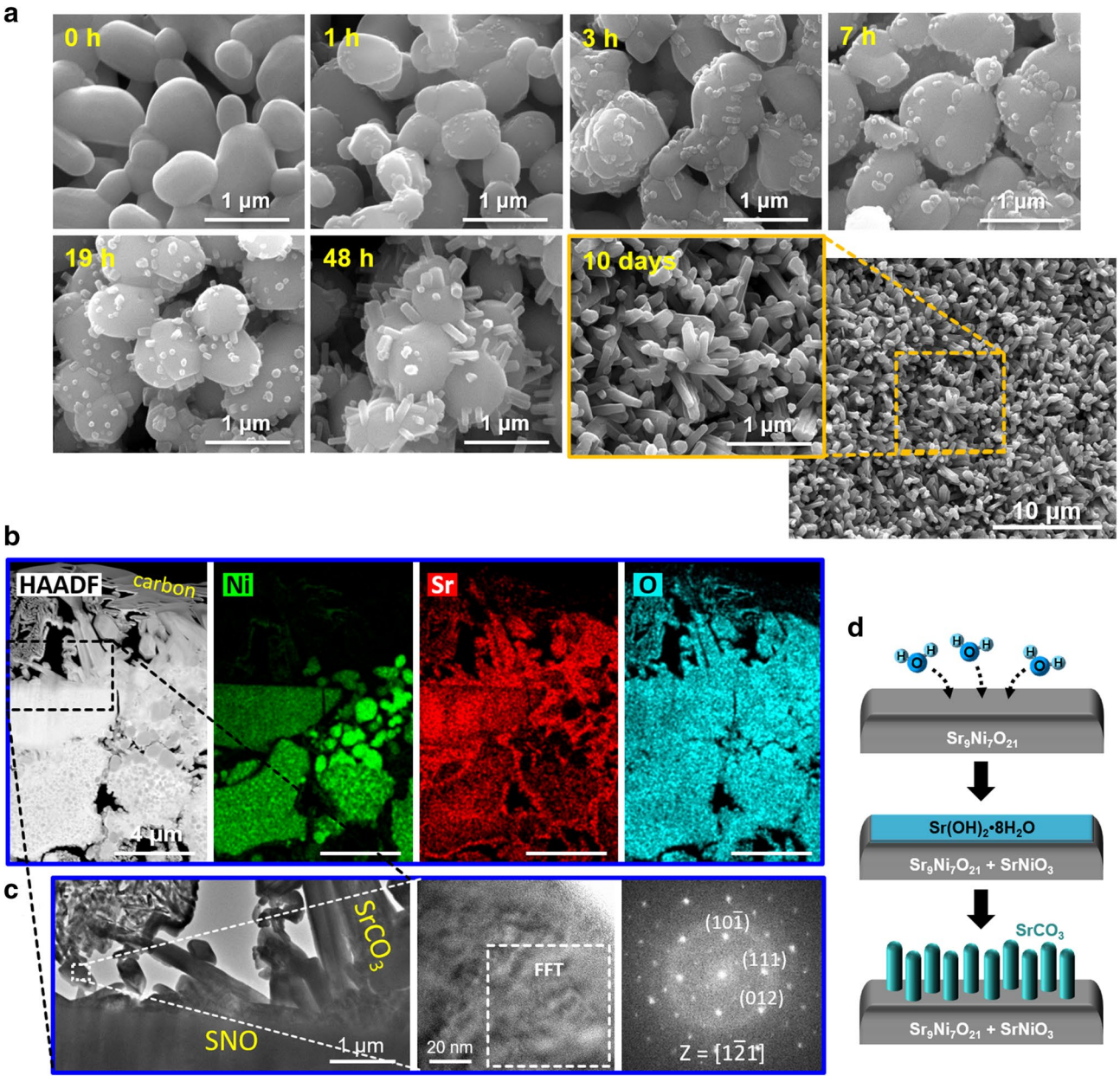

Figure 1. (**a**) SEM images of the surface of strontium nickel oxide pellet before and after the exposure to a humid environment (2.7% H_2O content) for 1 h, 3 h, 7 h, 19 h, 48 h, and 10 days. The SEM–EDS spectrum of the nanorod array is also presented in Supplementary Fig. S2 online. It is noted that these samples were dried in ambient air (0.3% H_2O content) for 2 h after exposure to the humid environment. SEM images of the samples that were not dried are also displayed in Supplementary Fig. S3 online. (**b**) High-angle annular dark-field (HAADF) and elemental mapping images (Ni, Sr, and O) of the cross-section of the SNO pellet exposed to the humid environment for 5 days, analyzed using FIB and STEM-EDS. (**c**) High-resolution TEM images of the nanorod grown on the SNO surface and the corresponding FFT pattern indexed in the *Pmcn* space group of $SrCO_3$. (**d**) Schematic representation of the structural evolution of SNO by hydration and the accompanying $SrCO_3$ nanorod growth.

make an incorrect conclusion that the $SrCO_3$ crystal grows mainly along the (111) face[41,44]. However, such XRD pattern (at ~25.5° in Fig. 3c) is likely due to the broadening and overlapping of (111) and (021) peaks, rather than to the (111) oriented growth, which is in good agreement with the XRD profile simulated as a function of $SrCO_3$ crystallite sizes (see Supplementary Fig. S5 online). Since the peaks for (002), (113) and (023) planes, as shown in Fig. 3c, have much stronger intensities than those of typical $SrCO_3$ (Supplementary Fig. S6 online), those planes can be nominated as the preferred orientation of the $SrCO_3$ growth. Next, XRD simulations on the planes were performed using CrystalDiffract software to identify the preferred orientation plane. Figure 4a displays simulated XRD patterns of the $SrCO_3$ with (002) preferred orientation as a function of the degree of alignment. It is found that the intensity of (113)/(023) peak increases, along with (002) peak, as shown in the

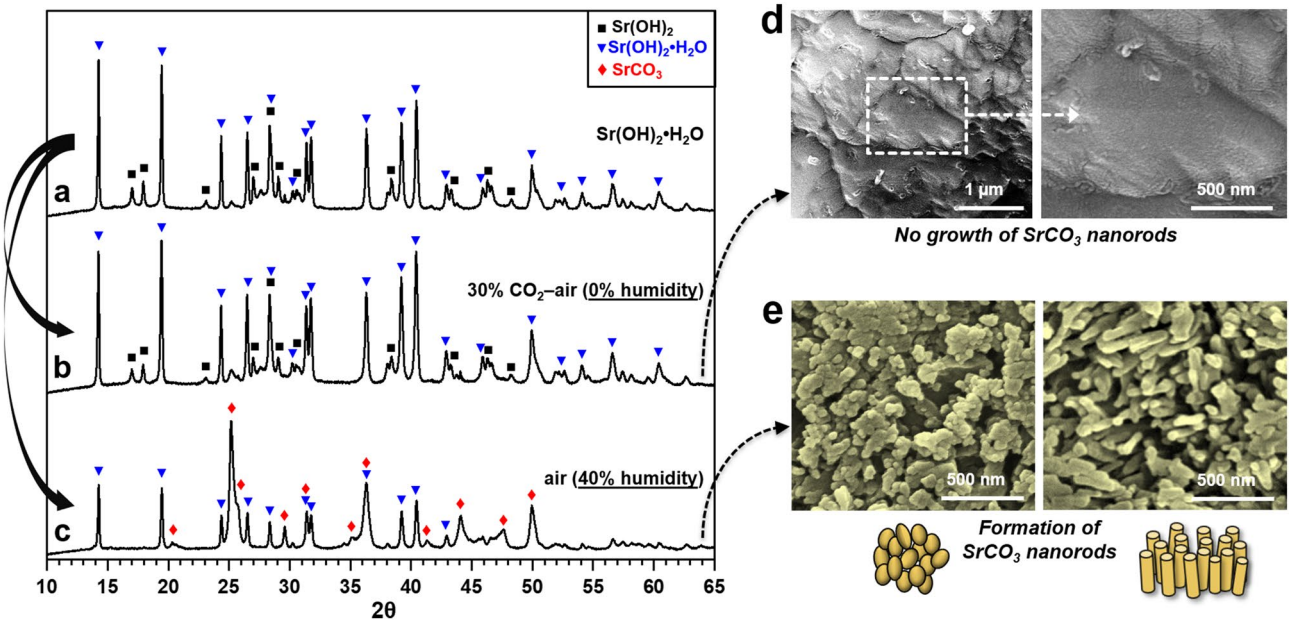

Figure 2. XRD patterns of SrO before and after exposure to ambient room air (1.2% H_2O present, and 400 ppm CO_2) and a CO_2-air mixed gas (H_2O absent, and 30% CO_2) for 24 h (**a**–**c**), and their corresponding SEM images (**d**,**e**). Note that the XRD pattern of SrO could not be properly recorded because SrO was readily hydrated by absorbing airborne moisture in the middle of XRD analysis; thus, $Sr(OH)_2$ and $Sr(OH)_2{\cdot}H_2O$ were detected instead of SrO.

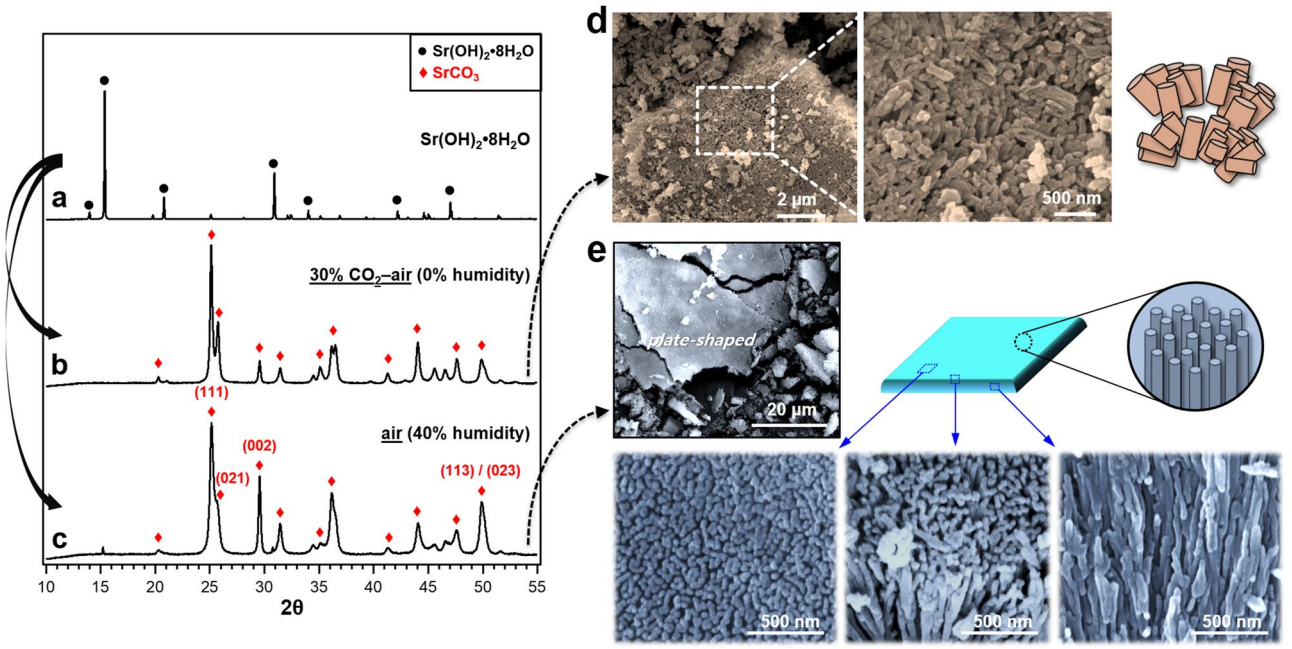

Figure 3. XRD patterns of $Sr(OH)_2{\cdot}8H_2O$ before and after exposure to an ambient room air (1.2% H_2O present, and 400 ppm CO_2) and a CO_2-air mixed gas (H_2O absent, and 30% CO_2) for 24 h (**a**–**c**), and their corresponding SEM images (**d**,**e**).

XRD patterns of the $SrCO_3$ with preferred orientation in (002) plane (Fig. 4a: right insets). This simulation result is well matched to the measured one in Fig. 3c, suggesting that the $SrCO_3$ nanorod grows preferentially at ⟨001⟩ direction (i.e., along *c*-axis).

TEM analysis was performed to further validate the above results. Figure 4b,c show SEM and TEM images of nanorods grown from $Sr(OH)_2{\cdot}8H_2O$ in humid condition. The low- and high-resolution (HR) TEM images of a single nanorod in Fig. 4d,e show fringes parallel to the growth direction of the nanorod (marked by arrows), indicative of planar defects. The FFT patterns of selected areas in Fig. 4e are displayed in Fig. 4f–h. The diffraction

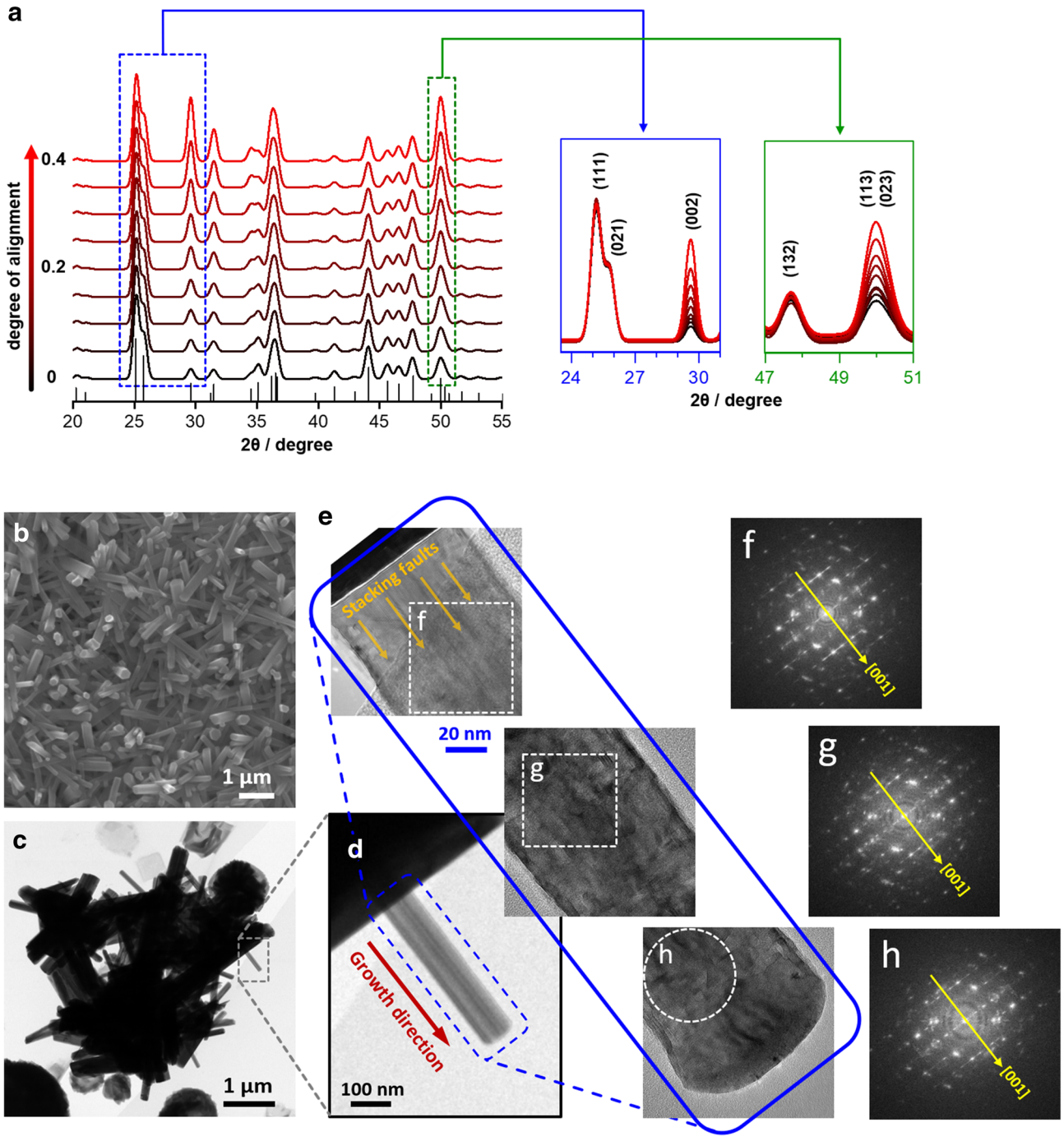

Figure 4. (**a**) Simulated XRD patterns of the $SrCO_3$ (*Pmcn*; orthorhombic; and D = 14 nm) with the preferred orientation along (002) plane (i.e., *c*-axis) as a function of the degree of alignment. The degree of alignment is represented by a fraction, with 0 indicating a completely random-oriented structure, and 1 being a fully oriented structure (e.g., precisely parallelly aligned rods). (**b**) SEM and (**c**) TEM images of $SrCO_3$ nanorods. (**d**,**e**) Low- and high-magnification TEM images of a single-crystalline $SrCO_3$ nanorod. (**f**–**h**) FFT diffraction patterns of selected areas in (**e**), indexed to the orthorhombic $SrCO_3$ (*Pmcn*; JCPDS No. 05-0418) (Supplementary Fig. S7 online).

spots are indexed to the orthorhombic $SrCO_3$ (*Pmcn*; JCPDS No. 05-0418) where the streaks, lying parallel to the [010] direction, reflect local disorder of the atomic stacking (i.e., stacking faults) as being perpendicular to the fringes in the HR-TEM image (see Supplementary Fig. S7 online). The distance between the streaks, normal to the growth direction, corresponds to the (001) plane, i.e., 0.60 nm, demonstrating the growth direction of the nanorod to be ⟨001⟩. Note that this kind of pattern appears in all regions of the nanorod (Fig. 4f–h). Hence, it is concluded that the $SrCO_3$ nuclei tend to assemble along the *c*-axis leaving stacking faults behind, which is in good agreement with the result from XRD simulation.

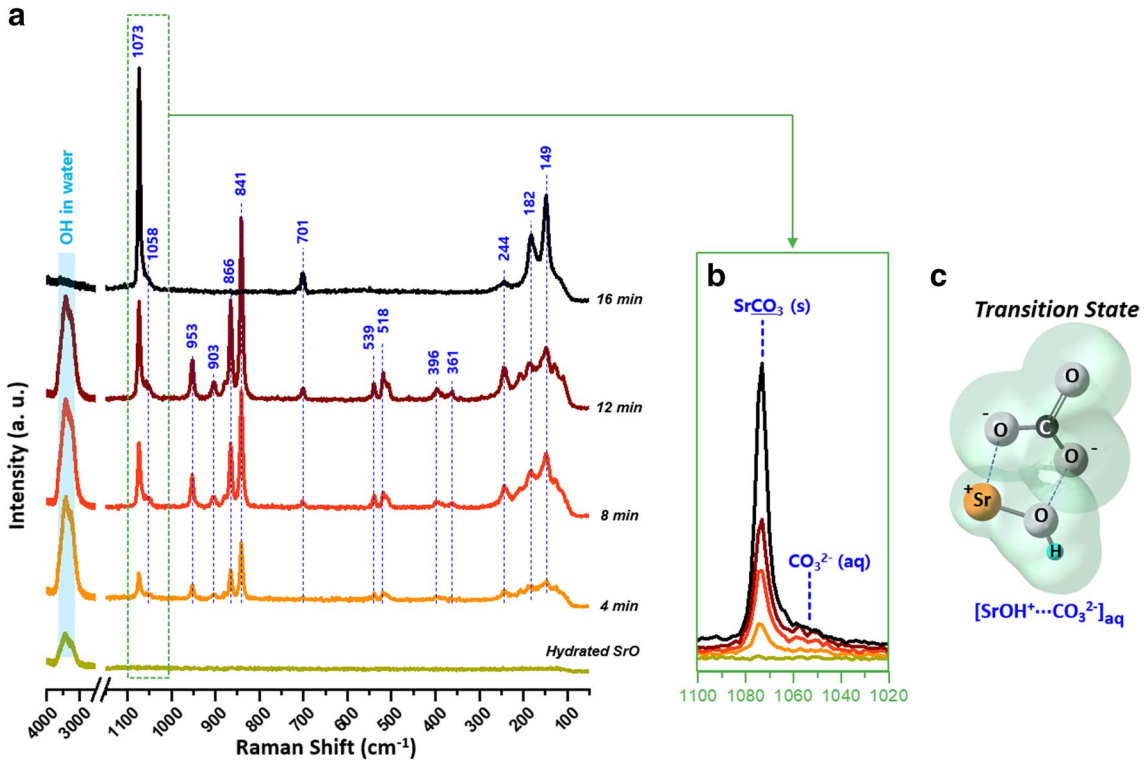

Figure 5. (**a**) Raman spectra of hydrated SrO in ambient air, recorded over time (0, 4, 8, 12, and 16 min). (**b**) Superimposed Raman spectra at the range of 1020–1100 cm^{-1}. (**c**) A structure of the transition-state intermediate, $SrOH^{+}\cdots CO_3^{2-}$. Vibration modes of the Raman spectra are displayed in Supplementary Table S2.

Chemical structure evolution of hydrated SrO to $SrCO_3$. The reaction pathway for the carbonation of hydrated SrO was investigated by in situ Raman spectroscopy. Figure 5 shows representative Raman spectra of hydrated SrO that is exposed to ambient air for up to 16 min. Vibration modes of the Raman spectra are displayed in Supplementary Table S2, according to literature[45–62].

The initial Raman spectrum of SrO soaked with water (Fig. 5a: Hydrated SrO) is dominated by a broad band at 3000–3700 cm^{-1} owing to the stretching of O–H in water[46], implying hydration of SrO. Over time, the peaks ascribable to $SrCO_3$ (149, 182, 244, 701, and 1073 cm^{-1}) rise, indicating the carbonation of hydrated strontium (Fig. 5a: 4–16 min). Careful observations on the peak for $SrCO_3$ at 1020–1100 cm^{-1} (Fig. 5b) reveal that the growth of the $SrCO_3$ peak is accompanied by the rise of the small band at ~ 1055 cm^{-1} (assigned to CO_3^{2-} ions in aqueous solution[51,52]) which is not present in the normal spectrum of solid $SrCO_3$ (see Supplementary Fig. S8 online). The results demonstrate that (i) hydrated strontium has a high tendency to absorb CO_2 and (ii) the absorbed CO_2 is present as CO_3^{2-} ions which are supposed to react with strontium to form $SrCO_3$. These results are supported by the facts that aqueous alkaline-earth-metal hydroxide solutions are strong bases (e.g., pH = 11.27–13.09 at 1–100 mM $Sr(OH)_2$) and that the basic solution has the high solubility of CO_2 (supposed to convert to CO_3^{2-}) thus capturing airborne CO_2 so as to meet the equilibrium condition. For details, see Supplementary Fig. S9 online.

While the dissolved carbon is present as CO_3^{2-} in the basic aqueous solution, the chemical structure of strontium has not been completely determined so far; for instance, the Sr^{2+} coordination number surrounded by H_2O/OH^- was variously suggested to be six, or eight, etc.[63–73]. Aside from such discrepancy, there is a general consensus that hydrated Sr^{2+} clusters have flexible structures freely exchanging H_2O and OH^- between the first and second shells[74,75]. This indicates that Sr^{2+} hydroxide clusters with Sr^{2+}–OH^- interaction (mostly mono/di-hydroxides[75]) are always present in high pH aqueous solutions (OH^- abundant); however, Sr^{2+} and OH^- are not directly connected in both $Sr(OH)_2{\cdot}8H_2O$ and $Sr(H_2O)_7(OH)^+$ solid phases (instead, only Sr^{2+}–H_2O interaction exists unless further hydrated)[69,76].

This assumption is thermodynamically reasonable. Figure 6 displays Gibbs free energies for the plausible reactions of strontium hydroxide and carbon ions in aqueous solution. Based on the Gibbs free energy changes of the formation of $SrOH^+$ and Sr^{2+} ions (red and orange curves in Fig. 6, respectively), it is energetically favorable for Sr^{2+} to be paired with OH^-, namely $SrOH^+$, which corresponds to the computational study[64,77]. After many attempts, $SrOH^+$ was indeed observed by in situ Raman spectroscopy. The signals attributable to $SrOH^+$ (bands at 361, 396, 518, and 539 cm^{-1}) and to O–O stretching in $Sr(O_2)_{1-x}$–O_x (bands at 840–860 cm^{-1}) were detected (Fig. 5a: 4 min). The intensity of the bands relating to $SrOH^+$, $Sr(O_2)_{1-x}$–O_x, and $SrCO_3$ increased simultaneously during the Sr-carbonation (Fig. 5a: 4–12 min). After completion of the carbonation (Fig. 5a: 16 min), the bands disappeared, leaving only those for $SrCO_3$. These findings indicate that $SrOH^+$–CO_3^{2-}, or $SrHO^+$–OCO_2^{2-} (depicted in Fig. 5c), is an intermediate phase during the carbonation of hydrated strontium.

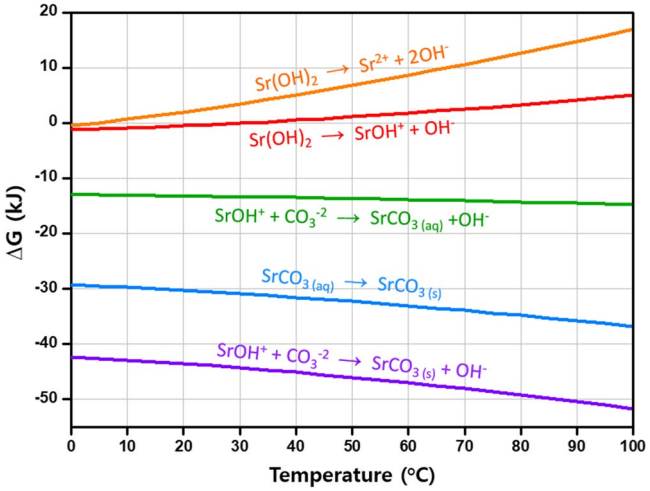

Figure 6. Gibbs free energy changes for the plausible reactions of strontium hydroxide and carbon ions in aqueous solution at 0–100 °C, plotted using HSC Chemistry software.

It is thus evident that, in the Sr liquid droplets, the interaction of CO_3^{2-} with $SrOH^+$ in $Sr(OH)_x(H_2O)_y$ cluster orients the $SrCO_3$ nuclei, and subsequent dehydration leaves $SrCO_3$ nanorods.

Discussion

We have studied water-mediated Sr-precipitate and growth of strontianite nanorod arrays on the surface of strontium compounds in ambient conditions. As a case study, we choose to investigate $Sr_9Ni_7O_{21}$, which is a Cr gettering material[78]. The compound is prone to Sr-segregation in air by absorbing airborne moisture and transforming the structure as per the reaction: $Sr_9Ni_7O_{21} + nH_2O \rightarrow 7SrNiO_3 + 2Sr(OH)_2{\cdot}8H_2O$. The segregated $Sr(OH)_2{\cdot}8H_2O$ subsequently converts to $SrCO_3$ in ambient air, which interestingly has nanorod morphology. Time-dependent SEM analysis demonstrated that the growth of $SrCO_3$ occurs in one direction when derived from hydrated SrO, such as $Sr(OH)_2{\cdot}8H_2O$.

The effect of water molecules on the formation and growth of $SrCO_3$ during the carbonation has been elucidated. In the absence of water molecules, SrO does not react with CO_2 even under high CO_2 partial pressure (30%), whereas SrO readily reacts with CO_2 in ambient air (water molecule present) despite its low concentration (400 ppm). These results suggest that the carbonation of SrO at ordinary temperatures occurs via hydration in the presence of moisture, as illustrated in Supplementary Fig. S10 online. The driving force for the Sr-carbonation can be understood from the perspective of CO_2 dissolution in aqueous alkaline solution. Basically, aqueous alkaline solutions have high solubility of carbonate ions due to high pH (i.e., high concentration of OH^-). Likewise, the moisture absorption endows strontium with more alkaline character, and thus the hydrated strontium, such as $Sr(OH)_2{\cdot}8H_2O$ and $Sr(OH)_2{\cdot}xH_2O$, becomes capable of absorbing CO_2 in air. In the alkaline condition of hydrated strontium, Sr^{2+} is likely to be coupled with OH^- (i.e., $SrOH^+$), and the absorbed CO_2 converts into CO_3^{2-}. Subsequent interaction of the Sr and C ions leads to the formation of $SrCO_3$ nuclei (Supplementary Fig. S10 online). Hence, the generally known fact "SrO is likely to react with CO_2" can be better understood as "Once hydrated, SrO reacts with CO_2".

It is also found that the morphology of the resulting $SrCO_3$ is affected by the kinetics of $SrCO_3$ formation. The Sr-carbonation via hydration is known to occur following the reaction, $Sr(OH)_2{\cdot}8H_2O + CO_2 \rightarrow SrCO_3 + 9H_2O$. It is thus implied that the kinetics of $SrCO_3$ formation is slower under low CO_2 and high H_2O partial pressures (or humidity level). Experimental results in Figs. 2 and 3 showed the growth trend of $SrCO_3$ under different atmospheric conditions. When $SrCO_3$ forms under high pCO_2 and low pH_2O (i.e., favorable for fast reaction kinetics), it has spherical morphology, suggesting the isotropic growth of $SrCO_3$. In contrast, when $SrCO_3$ forms under low pCO_2 and high pH_2O (i.e., desirable for slow reaction kinetics), it is likely to have nanorod morphology, indicating the anisotropic growth of $SrCO_3$. That is, the slower the reaction kinetics, the more the $SrCO_3$ grows in one direction (Supplementary Fig. S11 online). Thus, it is considered that, when sufficient time is given for precursor ions to move and rotate, anisotropic assembly occurs particularly along [001] direction resulting in *c*-axis oriented $SrCO_3$ nanorods.

The formation process of $SrCO_3$ nanorod arrays from Sr-enriched phases by vapor–liquid–solid mechanism in ambient conditions is summarized in Fig. 7. First, the Sr-terminated surface, being hygroscopic, attracts and absorbs water molecules in air (Fig. 7a). This leads to the hydration and segregation of strontium onto the surface, thus forming $Sr(OH)_2{\cdot}H_2O$, $Sr(OH)_2{\cdot}8H_2O$, and $Sr(OH)_x{\cdot}(H_2O)_y$ layers (Fig. 7b). The alkaline nature of the hydrated Sr-hydroxide layer causes the uptake of CO_2 in air, which subsequently converts to HCO_3^- and CO_3^{2-} (Fig. 7c). In the moistened medium, Sr and C ion complexes, including $SrOH^+$ and CO_3^{2-}, freely move, rotate, and interact with each other, leading to the assembly, nucleation, and growth of $SrCO_3$ (Fig. 7d). Particularly, the growth occurs preferentially along the *c*-axis, leaving staking faults behind. In this way, quasi-vertically aligned $SrCO_3$ nanorod arrays with (002) orientation can form at room temperature in ambient air without external addition of carbon source (Fig. 7e). This study paves the way for designing and developing 1D architecture

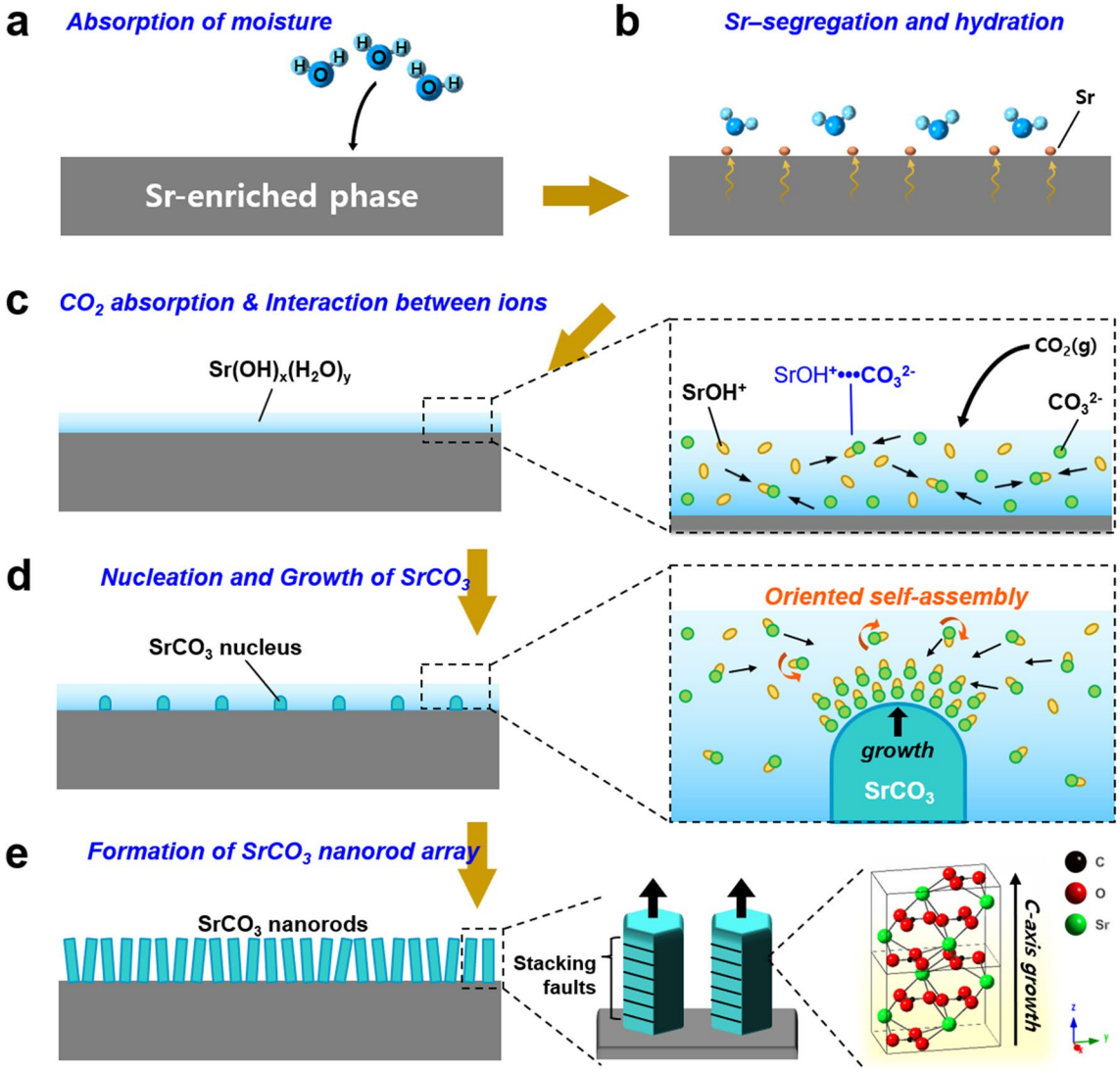

Figure 7. Schematic diagram for the process of the growth of $SrCO_3$ nanorod arrays from hydrated strontium that is segregated from Sr-containing substrates.

of $SrCO_3$ via H_2O-mediated precipitation from Sr-rich compounds. This strategy can also be applicable to other alkaline-earth-metal compounds to fabricate 1D nanostructures.

Methods

For the preparation of strontium nickel oxide ($Sr_9Ni_7O_{21}$), the mixtures of $Sr(OH)_2{\cdot}8H_2O$ (Sigma-Aldrich, USA) and $Ni(OH)_2$ (Sigma-Aldrich, USA) were heat-treated at 850–900 °C in air, where the molar ratio of Sr to Ni was 35:65 (see Ref.[14]). As-prepared SNO powder was uniaxially pressed into cylindrical pellets, followed by sintering at 900 °C. The SNO pellets were placed in a humid environment (i.e., a sealed container containing water at the bottom, 2.7% H_2O content measured by a ThermoPro hygrometer). The pellet surface, which was exposed to the humid environment for 0–48 h and 10 days, was examined by a field-emission environmental scanning electron microscope (FE-ESEM; Quanta 250 FEG, FEI, USA) equipped with an energy dispersive X-ray spectrometer (EDS), for which the specimens were coated with gold either after being dried for 2 h in ambient air or immediately after being taken out from the humid condition. For scanning transmission electron microscopy (STEM) analysis, the SNO pellet, exposed to the humid environment for 5 days, was sliced using a focused ion beam (FIB; Helios Nanolab 460F1, FEI, USA). The specimen was analyzed using STEM (Talos F200X S/TEM, FEI, USA).

The structures and morphologies of as-received SrO (Alfa Aesar, USA) and $Sr(OH)_2{\cdot}8H_2O$ (Sigma-Aldrich, USA), exposed either to an ambient atmosphere (with 400 ppm CO_2 and 1.2% H_2O contents) or to CO_2-air mixture (with 30% CO_2 and ~0% H_2O contents) at room temperature, were analyzed using SEM and X-ray diffractometer (XRD; D8 Advance, Bruker, Germany) with Cu-kα radiation (λ = 0.1542 nm). CrystalDiffract software (Version 6.8.2, CrystalMaker Software Ltd.) was used to identify and simulate XRD patterns of $SrCO_3$ nanorods with different growth directions. The following parameters were used in the simulation: *Pmcn* (orthorhombic); lattice constants a = 5.107 Å, b = 8.414 Å, and c = 6.029 Å; and crystallite size = 14 nm. TEM analysis (Talos

F200X S/TEM; FEI, USA) was performed on $SrCO_3$ nanorods grown from $Sr(OH)_2{\cdot}8H_2O$ in humid condition. For TEM sample preparation, the nanorods were dispersed in ethanol and dropped onto a carbon-coated grid. TEM images were obtained at an accelerating voltage of 200 kV, followed by fast-Fourier-transformation analysis.

For in situ monitoring of the growth of $SrCO_3$ from hydrated SrO, Raman spectroscopy (Ramanscope 2000, Renishaw, Gloucestershire, UK) was employed. As-received SrO particles were drenched in a droplet of DI water on a microscope glass slide to form an aqueous film of strontium hydroxide hydrate. Raman spectra of the film were then recorded over time with a laser of 514.5 nm wavelength. Gibbs free energy changes for the probable reactions between strontium and carbon ions at 0–100 °C were calculated from the database in HSC Chemistry 6 (Outotec, Finland).

Received: 10 March 2020; Accepted: 18 January 2021
Published online: 09 February 2021

References

1. Ropp, R. C. Encyclopedia of the alkaline earth compounds. *Elsevier* https://doi.org/10.1016/B978-0-444-59550-8.00013-2 (2013).
2. McDaniel, A. H. *et al.* Sr- and Mn-doped $LaAlO_{3-\delta}$ for solar thermochemical H_2 and CO production. *Energy Environ. Sci.* **6**, 2424–2428 (2013).
3. Suntivich, J. *et al.* Design principles for oxygen-reduction activity on perovskite oxide catalysts for fuel cells and metal-air batteries. *Nat. Chem.* **3**, 546–550 (2011).
4. Kawasaki, S., Kamata, K. & Hara, M. Dioxygen activation by a hexagonal $SrMnO_3$ perovskite catalyst for aerobic liquid-phase oxidation. *ChemCatChem* **8**, 3247–3253 (2016).
5. van Roosmalen, J. A. M., Huijsmans, J. P. P. & Plomp, L. Electrical conductivity in $La_{1-x}Sr_xMnO_{3+\delta}$. *Solid State Ionics* **66**, 279–284 (1993).
6. Kuo, J. H., Anderson, H. U. & Sparlin, D. M. Oxidation-reduction behavior of undoped and Sr-doped $LaMnO_3$: Defect structure, electrical conductivity, and thermoelectric power. *J. Solid State Chem.* **87**, 55–63 (1990).
7. Aruna, S. T., Muthuraman, M. & Patil, K. C. Combustion synthesis and properties of strontium substituted lanthanum manganites $La_{1-x}Sr_xMnO_3$ ($0 \le x \le 0.3$). *J. Mater. Chem.* **7**, 2499–2503 (1997).
8. Nagde, K. R. & Bhoga, S. S. Effect of Sr content on structure and electrical properties of $La_{1-x}Sr_xMnO_3$ from ITSOFC cathode view point. *Ionics* **15**, 571–578 (2009).
9. Lee, W., Han, J. W., Chen, Y., Cai, Z. & Yildiz, B. Cation size mismatch and charge interactions drive dopant segregation at the surfaces of manganite perovskites. *J. Am. Chem. Soc.* **135**, 7909–7925 (2013).
10. Yu, Y. *et al.* Effect of Sr content and strain on Sr surface segregation of $La_{1-x}Sr_xCo_{0.2}Fe_{0.8}O_{3-\delta}$ as cathode material for solid oxide fuel cells. *ACS Appl. Mater. Interfaces* **8**, 26704–26711 (2016).
11. Koo, B. *et al.* Sr segregation in perovskite oxides: Why it happens and how it exists. *Joule* **2**, 1476–1499 (2018).
12. Bachelet, R., Sánchez, F., Palomares, F. J., Ocal, C. & Fontcuberta, J. Atomically flat SrO-terminated $SrTiO_3$ (001) substrate. *Appl. Phys. Lett.* **95**, 141915 (2009).
13. Xu, C. *et al.* Formation mechanism of Ruddlesden–Popper-type antiphase boundaries during the kinetically limited growth of Sr rich $SrTiO_3$ thin films. *Sci. Rep.* **6**, 1–8 (2016).
14. Oudah, M. *et al.* Evolution of superconductivity with Sr-deficiency in antiperovskite oxide $Sr_{3-x}SnO$. *Sci. Rep.* **9**, 1–9 (2019).
15. Halwidl, D. *et al.* Adsorption of water at the SrO surface of ruthenates. *Nat. Mater.* **15**, 450–455 (2016).
16. Hong, J., Heo, S. J., Aphale, A. N., Hu, B. & Singh, P. H_2O absorption assisted Sr-segregation in strontium nickel oxide based chromium getter and encapsulation with $SrCO_3$. *J. Electrochem. Soc.* **166**, F59–F65 (2019).
17. Hu, B., Keane, M., Mahapatra, M. K. & Singh, P. Stability of strontium-doped lanthanum manganite cathode in humidified air. *J. Power Sources* **248**, 196–204 (2014).
18. Zhang, G., Verdugo-Escamilla, C., Choquesillo-Lazarte, D. & García-Ruiz, J. M. Thermal assisted self-organization of calcium carbonate. *Nat. Commun.* **9**, 1–7 (2018).
19. Wang, S., Zhang, X., Zhou, G. & Wang, Z. S. Double-layer coating of $SrCO_3/TiO_2$ on nanoporous TiO_2 for efficient dye-sensitized solar cells. *Phys. Chem. Chem. Phys.* **14**, 816–822 (2012).
20. Rhodes, N. R. *et al.* Solar thermochemical energy storage through carbonation cycles of $SrCO_3$/SrO supported on $SrZrO_3$. *Chemsuschem* **8**, 3793–3798 (2015).
21. Zhang, Q., Meng, F., Zha, L., Wang, X. & Zhang, G. A sensitive cataluminescence-based sensor using a $SrCO_3$/graphene composite for n-propanol. *RSC Adv.* **5**, 57482–57489 (2015).
22. Ghouri, Z. K., Elsaid, K., Al-Meer, S. & Barakat, N. A. M. Applicable anode based on Co_3O_4–$SrCO_3$ heterostructure nanorods-incorporated CNFs with low-onset potential for DUFCs. *Appl. Nanosci.* **7**, 625–631 (2017).
23. Song, L., Zhang, S. & Chen, B. A novel visible-light-sensitive strontium carbonate photocatalyst with high photocatalytic activity. *Catal. Commun.* **10**, 1565–1568 (2009).
24. Jin, J., Chen, S., Wang, J., Chen, C. & Peng, T. $SrCO_3$-modified brookite/anatase TiO_2 heterophase junctions with enhanced activity and selectivity of CO_2 photoreduction to CH_4. *Appl. Surf. Sci.* **476**, 937–947 (2019).
25. Jin, S., Dong, G., Luo, J., Ma, F. & Wang, C. Improved photocatalytic NO removal activity of $SrTiO_3$ by using $SrCO_3$ as a new co-catalyst. *Appl. Catal. B Environ.* **227**, 24–34 (2018).
26. Wang, Z., He, G., Yin, H., Bai, W. & Ding, D. Evolution of controllable urchin-like $SrCO_3$ with enhanced electrochemical performance via an alternative processing. *Appl. Surf. Sci.* **411**, 197–204 (2017).
27. Li, J. M. Realizing single-crystalline vertically-oriented and high-density electrospun nanofibril bundles by controlled postcalcination. *CrystEngComm* **19**, 3392–3397 (2017).
28. Sreedhar, B., Sulochana, M., Vani, C. S., Devi, D. K. & Naidu, N. V. S. Shape evolution of strontium carbonate architectures using natural gums as crystal growth modifiers. *Eur. Chem. Bull.* **3**, 234–239 (2014).
29. Alavi, M. A. & Morsali, A. Syntheses and characterization of $Sr(OH)_2$ and $SrCO_3$ nanostructures by ultrasonic method. *Ultrason. Sonochem.* **17**, 441–446 (2010).
30. Yu, J., Guo, H. & Cheng, B. Shape evolution of $SrCO_3$ particles in the presence of poly-(styrene-alt-maleic acid). *J. Solid State Chem.* **179**, 800–803 (2006).
31. Li, S., Zhang, H., Xu, J. & Yang, D. Hydrothermal synthesis of flower-like $SrCO_3$ nanostructures. *Mater. Lett.* **59**, 420–422 (2005).
32. Guo, G. S., Gu, F. B., Wang, Z. H. & Guo, H. Y. Low-temperature growth of single-crystal $SrCO_3$ nanoneedles. *Chin. Chem. Lett.* **16**, 1101–1104 (2005).
33. Jahangiri, H., Ranjbar, M., Taher, M. A. & Kazerooni, H. Using microwave heating for synthesis of $SrCO_3$ nanostructures with different morphologies. *J. Ind. Eng. Chem.* **21**, 1132–1136 (2015).
34. Cao, M., Wu, X., He, X. & Hu, C. Microemulsion-mediated solvothermal synthesis of $SrCO_3$ nanostructures. *Langmuir* **21**, 6093–6096 (2005).

35. Arumugam, D. *et al.* Growth mechanism of pine-leaf-like nanostructure from the backbone of $SrCO_3$ nanorods using LaMer's surface diffusion: Impact of higher surface energy (γ = 38.9 eV/nm^2) {111} plane stacking along ⟨110⟩ (γ = 3.4 eV/nm^2) by first-principles calculations. *Cryst. Growth Des.* **17**, 6394–6406 (2017).
36. Yang, L., Chu, D., Wang, L., Ge, G. & Sun, H. Facile synthesis of porous flower-like $SrCO_3$ nanostructures by integrating bottom-up and top-down routes. *Mater. Lett.* **167**, 4–8 (2016).
37. Wang, W. S., Zhen, L., Xu, C. Y., Yang, L. & Shao, W. Z. Room temperature synthesis of hierarchical $SrCO_3$ architectures by a surfactant-free aqueous solution route. *Cryst. Growth Des.* **8**, 1734–1740 (2008).
38. Rautaray, D., Sanyal, A., Adyanthaya, S. D., Ahmad, A. & Sastry, M. Biological synthesis of strontium carbonate crystals using the fungus Fusarium oxysporum. *Langmuir* **20**, 6827–6833 (2004).
39. Guo, G., Yan, G., Wang, L. & Huang, J. Crystallization of strontium carbonate in alcohol or water solution containing mixed nonionic/anionic surfactants. *Mater. Lett.* **62**, 4018–4021 (2008).
40. Liao, F., Zhao, L., Zhai, C., Zhang, Z. & Ma, X. Morphology and photoluminescence properties of $SrCO_3$ prepared by a simple solution method. *Mater. Lett.* **122**, 331–333 (2014).
41. Zhang, W., Yu, Y. & Yi, Z. Controllable synthesis of $SrCO_3$ with different morphologies and their co-catalytic activities for photo-catalytic oxidation of hydrocarbon gases over TiO_2. *J. Mater. Sci.* **52**, 5106–5116 (2017).
42. Han, Y., Nishimura, T. & Kato, T. Biomineralization-inspired approach to the development of hybrid materials: Preparation of patterned polymer/strontium carbonate thin films using thermoresponsive polymer brush matrices. *Polym. J.* **46**, 499–504 (2014).
43. Hong, J. *et al.* Strontium manganese oxide getter for capturing airborne Cr and S contaminants in high-temperature electrochemical systems. *ACS Appl. Mater. Interfaces* **11**, 34878–34888 (2019).
44. Sreedhar, B. *et al.* Bioinspired synthesis of morphologically controlled $SrCO_3$ superstructures by natural gum acacia. *Cryst. Res. Technol.* **46**, 485–492 (2011).
45. Sun, Q. The Raman OH stretching bands of liquid water. *Vib. Spectrosc.* **51**, 213–217 (2009).
46. Carey, D. M. & Korenowski, G. M. Measurement of the Raman spectrum of liquid water. *J. Chem. Phys.* **108**, 2669–2675 (1998).
47. Slodczyk, A., Tran, C. & Colomban, P. Face to face with enemy—analysis of aqua carbonate hydroxide second surface phases in proton conducting perovskite ceramic electrolytic membrane. *Mater. Res. Soc. Symp. Proc.* **1384** (2012).
48. Colomban, P., Tran, C., Zaafrani, O. & Slodczyk, A. Aqua oxyhydroxycarbonate second phases at the surface of Ba/Sr-based proton conducting perovskites: A source of confusion in the understanding of proton conduction. *J. Raman Spectrosc.* **44**, 312–320 (2013).
49. Lutz, H. D., Eckers, W., Schneider, G. & Haeuseler, H. Raman and infrared spectra of barium and strontium hydroxides and hydroxide hydrates. *Spectrochim. Acta Part A Mol. Spectrosc.* **37**, 561–567 (1981).
50. Wehrmeister, U., Soldati, A. L., Jacob, D. E., Häger, T. & Hofmeister, W. Raman spectroscopy of synthetic, geological and biological vaterite: A Raman spectroscopic study. *J. Raman Spectrosc.* **41**, 193–201 (2010).
51. Wen, N. & Brooker, M. H. Ammonium carbonate, ammonium bicarbonate, and ammonium carbamate equilibria: A raman study. *J. Phys. Chem.* **99**, 359–368 (1995).
52. Idris, Z., Jens, K. J. & Eimer, D. A. Speciation of MEA-CO_2 adducts at equilibrium using Raman spectroscopy. *Energy Procedia* **63**, 1424–1431 (2014).
53. Upasen, S., Batocchi, P., Mauvy, F., Slodczyk, A. & Colomban, P. Chemical and structural stability of $La_{0.6}Sr_{0.4}Co_{0.2}Fe_{0.8}O_{3-\delta}$ ceramic vs medium/high water vapor pressure. *Ceram. Int.* **41**, 14137–14147 (2015).
54. de Waal, D., Range, K.-J., Königstein, M. & Kiefer, W. Raman spectra of the barium oxide peroxide and strontium oxide peroxide series. *J. Raman Spectrosc.* **29**, 109–113 (1998).
55. Xie, S., Mestl, G., Rosynek, M. P. & Lunsford, J. H. Decomposition of nitric oxide over barium oxide supported on magnesium oxide. 1. Catalytic results and in situ Raman spectroscopic evidence for a barium-nitro intermediate. *J. Am. Chem. Soc.* **119**, 10186–10191 (1997).
56. Eysel, H. H. & Thym, S. Raman spectra of peroxides. *J. Inorg. Gen. Chem.* **411**, 97–102 (1975).
57. Mestl, G., Rosynek, M. P. & Lunsford, J. H. Decomposition of nitric oxide over barium oxide supported on magnesium oxide. 4. In situ Raman characterization of oxide phase transitions and peroxide species by 18 O-labeling. *J. Phys. Chem. B* **102**, 154–161 (1998).
58. Bonales, L. J. *et al.* Quantitative Raman spectroscopy as a tool to study the kinetics and formation mechanism of carbonates. *Spectrochim. Acta Part A Mol. Biomol. Spectrosc.* **116**, 26–30 (2013).
59. Tavender, S. M., Johnson, S. A., Balsom, D., Parker, A. W. & Bisby, R. H. The carbonate, CO_3^-, in solution studied by resonance Raman spectroscopy. *Laser Chem.* **19**, 311–316 (1999).
60. Brazier, C. R. & Bernath, P. F. Laser and Fourier transform spectroscopy of the Ã2II-X̃2Σ+ transition of SrOH. *J. Mol. Spectrosc.* **114**, 163–173 (1985).
61. Buzgar, N. & Apopei, A. I. The Raman study of certain carbonates. *Geol. Tomul LV* **2**, 97–112 (2009).
62. Krishnan, T. S. Raman spectrum of strontianite ($SrCO_3$). *Proc. Indian Acad. Sci. Sect. A* **44**, 96–98 (1956).
63. Axe, L., Bunker, G. B., Anderson, P. R. & Tyson, T. A. An XAFS analysis of strontium at the hydrous ferric oxide surface lisa. *J. Colloid Interface Sci.* **52**, 44–52 (1998).
64. Kerridge, A. & Kaltsoyannis, N. The coordination of Sr^{2+} by hydroxide: A density functional theoretical study. *Dalt. Trans.* **40**, 11258–11266 (2011).
65. Persson, I., Sandström, M., Yokoyama, H. & Chaudhry, M. Structure of the solvated strontium and barium ions in aqueous, dimethyl sulfoxide and pyridine solution, and crystal structure of strontium and barium hydroxide octahydrate. *J. Phys. Sci. A* **50**, 21–37 (1995).
66. D'Angelo, P., Nolting, H. F. & Pavel, N. V. Evidence for multielectron resonances at the Sr K edge. *Phys. Rev. A* **53**, 798–805 (1996).
67. Kerridge, A. & Kaltsoyannis, N. Quantum chemical studies of the hydration of Sr^{2+} in vacuum and aqueous solution. *Chem. Eur. J.* **17**, 5060–5067 (2011).
68. Albright, J. N. X-ray diffraction studies of aqueous alkaline-earth chloride solutions. *J. Chem. Phys.* **56**, 3783–3786 (1972).
69. Felmy, A. R., Dixon, D. A., Rustad, J. R., Mason, M. J. & Onishi, L. M. The hydrolysis and carbonate complexation of strontium and calcium in aqueous solution. Use of molecular modeling calculations in the development of aqueous thermodynamic models. *J. Chem. Thermodyn.* **30**, 1103–1120 (1998).
70. Caminiti, R., Musinu, A., Paschina, G. & Pinna, G. X-ray diffraction study of aqueous $SrCl_2$ solutions. *J. Appl. Crystallogr.* **15**, 482–487 (1982).
71. Glendening, E. D. & Feller, D. Dication–Water interactions: $M^{2+}(H_2O)_n$ clusters for alkaline earth metals M = Mg, Ca, Sr, Ba, and Ra. *J. Phys. Chem.* **100**, 4790–4797 (1996).
72. Moreau, G., Helm, L., Purans, J. & Merbach, A. E. Structural investigation of the aqueous Eu^{2+} ion: Comparison with Sr^{2+} using the XAFS technique. *J. Phys. Chem. A* **106**, 3034–3043 (2002).
73. Harris, D. J., Brodholt, J. P. & Sherman, D. M. Hydration of Sr^{2+} in hydrothermal solutions from ab initio molecular dynamics. *J. Phys. Chem. B* **107**, 9056–9058 (2003).
74. D'Angelo, P., Migliorati, V., Sessa, F., Mancini, G. & Persson, I. XANES reveals the flexible nature of hydrated strontium in aqueous solution. *J. Phys. Chem. B* **120**, 4114–4124 (2016).
75. Makkos, E., Kerridge, A. & Kaltsoyannis, N. The importance of second shell effects in the simulation of hydrated Sr^{2+} hydroxide complexes. *Dalt. Trans.* **44**, 11572–11581 (2015).

76. Arcis, H., Zimmerman, G. H. & Tremaine, P. R. Ion-pair formation in aqueous strontium chloride and strontium hydroxide solutions under hydrothermal conditions by AC conductivity measurements. *Phys. Chem. Chem. Phys.* **16**, 17688–17704 (2014).
77. Makkos, E. *Computational Investigations of the Speciation of Sr^{2+} in Aqueous Solution, and Its Interactions with the Hydrated Brucite (0001) Surface in Aqueous Solution, and Its Interactions with the Hydrated Brucite (0001) Surface* (University College London, London, 2017).
78. Heo, S. J., Hong, J., Aphale, A., Hu, B. & Singh, P. Chromium poisoning of $La_{1-x}Sr_xMnO_{3\pm\delta}$ cathodes and electrochemical validation of chromium getters in intermediate temperature-solid oxide fuel cells. *J. Electrochem. Soc.* **166**, F990–F995 (2019).

Acknowledgements

The authors acknowledge financial support from US Department of Energy under research grant DE-FE-0023385. The Center for Clean Energy Engineering (C2E2) and the Institute of Materials Science (IMS) are acknowledged for X-ray diffraction and Raman spectroscopy analyses. We also thank Dr. Lichun Zhang (University of Connecticut) and Dr. Yong-Ryun Jo (Gwangju Institute of Science and Technology) for help with TEM analysis.

Author contributions

P.S. supervised the project. J.H. prepared all samples, and performed SEM, TEM, Raman, XRD, and thermodynamic analyses. J.H., S.J.H. and P.S. contributed to the discussion of results. J.H. wrote the manuscript. S.J.H. and P.S. commented and helped revise the manuscript.

Competing interests

The authors declare no competing interests.

Additional information

Supplementary Information The online version contains supplementary material available at https://doi.org/10.1038/s41598-021-82651-0.

Correspondence and requests for materials should be addressed to P.S.

Reprints and permissions information is available at www.nature.com/reprints.

Publisher's note Springer Nature remains neutral with regard to jurisdictional claims in published maps and institutional affiliations.